CHEMISTRY OF MATERIALS

pubs.acs.org/cm

Article

Design, Synthesis, and Evaluation of Noble Metal Nanoparticles and In Situ-Decorated Carbon-Supported Nanoparticle Electrocatalysts Using Hypergolic Reactions

Published as part of Chemistry of Materials special issue "In Memory of Prof. Francis DiSalvo".

Nikolaos Chalmpes, Iosif Tantis, Ahmed Wasel Alsmaeil, Athanasios B. Bourlinos, and Emmanuel P. Giannelis*

Cite This: https://doi.org/10.1021/acs.chemmater.4c02091

Read Online

ACCESS | Metrics & More | Article Recommendations | Supporting Information

ABSTRACT: We report the first synthesis of metal nanoparticles and supported metal nanoparticles on carbon by using hypergolic reactions. Specifically, we report the synthesis of noble metal nanoparticles (Pt, Ag, and Au) using sodium hydride (NaH) as both an ignition trigger and a reducing agent for the corresponding metal salt precursors. In addition, we report the one-step, in situ synthesis of Pt nanoparticles supported on carbon by adding sucrose as the carbon source. The hypergolically synthesized nanoparticles display elliptical morphology and are more crystalline compared with those conventionally synthesized in solution using sodium borohydride ($NaBH_4$). When tested as electrocatalysts, the hypergolic Pt nanoparticles exhibit more than 2 times higher specific electrochemical active surface area (ECSA) and a higher half-wave potential ($E_{1/2}$) of 0.94 V vs the reversible hydrogen electrode (RHE) compared to the conventionally synthesized ones. In addition, the electrocatalyst based on the in situ synthesized carbon that was decorated with the Pt nanoparticles synthesized hypergolically outperforms an analogous, state of the art, commercial PtC system. For example, the former shows an attractive $E_{1/2}$ (0.94 V) compared with 0.9 V for the commercial PtC. Accelerated durability tests (ADT) in an alkaline environment add another advantage. After 10 000 cycles, the hypergolically synthesized system shows a smaller reduction of $E_{1/2}$ and less degradation compared to the commercial PtC (10 mV compared to ∼30 mV). The work described here represents the first reported synthesis using hypergolic reactions of metal nanoparticles as well as supported metal nanoparticles. The properties of the resulting electrocatalysts demonstrate the versatility and promise of the new approach in materials synthesis and open new avenues for further investigation as electrocatalysts.

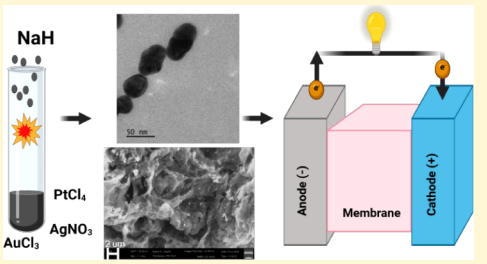

1. INTRODUCTION

Metal nanoparticles have become one of the most widely investigated fields of nanoscience and nanotechnology. Nanoparticles exhibit a wide range of unique properties that are significantly different compared to their bulk counterparts. Unique properties include a high surface-to-volume ratio resulting in a large fraction of surface atoms; quantum confinement; and highly tunable optical, electronic, and catalytic properties.[1,2] As a result, they have been researched for applications in various fields such as building blocks for various optoelectronic devices,[3] chemical sensing,[4] nanomedicine,[5−7] and drug delivery.[8]

Among them, noble metal nanoparticles (such as Pt, Pd, Ir, Rh, Ru, and Au) are at the center of research activity. The defect-rich surfaces along with their surface properties strongly influence their catalytic and electrocatalytic performance. In addition to their potential use as electrocatalysts,[9] noble metal nanoparticles have been proposed for use in other fields including infrared biosensing, bioimaging, photothermal therapy, and sensing.[10,11]

In general, noble metal nanoparticles are synthesized using two main approaches broadly defined as top-down or bottom-up approaches.[12] Top-down processes achieve structure sizes in the medium to lower nanometer range by breaking down bulk materials into entities of nanodimensions using physical or chemical methods. Top-down approaches include laser ablation, pyrolysis, chemical vapor deposition, and micropatterning.[13] In contrast, in the bottom-up approach, atomic or molecular units are assembled into nanoparticles through various processes using chemical and biological means.[14] Bottom-up approaches offer better control resulting in more uniform size and shape and controlled chemical composition.[15]

Received: July 26, 2024
Revised: October 7, 2024
Accepted: October 8, 2024

Examples of bottom-up approaches include reduction of metal ions in solution, electrochemical synthesis, and microemulsions with the former representing the most reliable and straightforward pathway to nanoparticles. In this process, the synthesis is accomplished by adding an appropriate reducing agent to the respective noble metal salt precursor(s). The list of reducing agents used includes sodium borohydride,[16] sodium citrate,[17] hydrazine,[18] tannic acid,[19] and others, with sodium borohydride being the most common.

Noble metal nanoparticles, especially platinum-based nanoparticles, are at the center of attention due to their favorable oxygen reduction reaction (ORR) performance. The most commonly used and commercialized electrode materials for both proton-exchange membrane fuel cells (PEMFCs) and anion-exchange membrane fuel cells (AEMFCs) are carbon-supported platinum electrocatalysts. For instance, the first fuel cell used in a vehicle (the Toyota Mirai) obtained a power of over 140 kW and a cruising range of more than 600 km.[20] Despite the favorable performance of these electrocatalysts, several critical challenges must be addressed before the technology is adopted more widely. First, the amount of Pt in the cathode has to be reduced without hindering the kinetics of ORR. Second, the Pt atom dissolution and migration during the electrochemical process should be minimized. Finally, the severe oxidation and corrosion of carbon during the electrochemical processes need to be addressed, since they lead to the detachment and aggregation of Pt particles, which accelerate the loss of ECSA.[21] For example, degradation of PtC catalysts during operation is among the reasons hindering the implementation of AEMFCs.[22] Therefore, producing PtC electrocatalysts with enhanced stability is an unmet need.

One of the ways to enhance the PtC electrochemical activity is to disperse the platinum nanoparticles on an optimal carbon support, which would not only increase the mass transfer and electrical conductivity of the catalytic layer but also contribute to the stabilization of metal nanoparticles.[23] The most common carbon supports include carbon blacks, such as Vulcan XC-72 and Ketjenblack. Unfortunately, up to now, there is still no clear information on the specific properties of the carbon support that address the stability issues and fulfill the above-mentioned needs.[24] Bayan et al. performed a comparative analysis of the PtC catalysts obtained on various carbon-based supports to identify the optimal candidate.[25] They tested the electrochemical characteristics of commercial Pt-decorated Ketjenblack and N-doped Ketjenblack as well as commercial carbon-supported Pt, PtC. The system based on Pt nanoparticles deposited on N-doped Ketjenblack showed the highest ECSA and ORR activity outperforming their commercial counterparts.[25]

Besides the carbon support, the characteristics of Pt nanoparticles can also influence the ORR efficiency. Development of novel Pt nanomaterials such as 1D Pt-based nanorods/wires/nanotubes, two-dimensional nanosheets, even three-dimensional (3D) networks, and porous superstructures have attracted widespread attention due to their excellent electrocatalytic activity and stability.[26] These multidimensional Pt nanosystems outperform the 0D Pt nanoparticles, since they are less vulnerable to dissolution, aggregation, and ripening due to their inherent anisotropic structure and low defect density.[27]

In this respect, hypergolic reactions recently proposed by our group as a new approach to the synthesis of various nanomaterials[28,29] offer an alternative pathway to synthesize metal nanoparticles. In general, hypergolic reactions are based on chemicals that ignite spontaneously upon contact in the absence of external stimuli such as pressure, temperature, and voltage. In those systems, the two required chemical substances are (a) a strong oxidizer media (e.g., fuming nitric acid) and (b) a fuel. The reaction typically is completed in a very short time of within a few seconds. Another clear differentiation compared to all the existing synthetic approaches, which are typically energy-consuming and require special reaction conditions, is the release of energy that can be converted into useful photovoltaic, thermoelectric, or mechanical work.[30,31] Such reactions have been exploited in rocket engineering and aircraft systems for propulsion and hydraulic power including defense aircraft, manned spacecraft, and deep space probes. Alternatively when used at a smaller scale, they offer a new and reliable synthetic approach toward the preparation of a wide range of nanomaterials.[32−34] Although synthesis of hypergolic materials shares some features with flame spray pyrolysis (FSP), it also exhibits some distinct differentiators. The most prominent is that in contrast to FSP, in which a flammable hydrocarbon (such as CH_4) is used to produce a flame, in hypergolic synthesis energy, it is released in situ from the reactants upon contact, eliminating the use of external energy inputs.[35,36]

In contrast to previously reported systems that led to various carbons by using fuming nitric acid as an oxidizing agent and a carbon source as the fuel, in this paper, we demonstrate for the first time the use of hypergolic reactions to synthesize metal nanoparticles. More specifically, we report here the first successful synthesis of Pt, Ag, and Au nanoparticles using sodium hydride (NaH) that has a dual role: as an exothermic ignition trigger and as a reducing agent of the corresponding metal precursor. In an effort to shed light on the synthesis mechanism, we compare samples synthesized hypergolically with the systems synthesized conventionally in solution using $NaBH_4$. The platinum nanoparticles were evaluated as ORR catalysts and benchmarked against commercial systems. Furthermore, owing to our interest in developing complete systems, we report as another first the in situ decoration of a carbon support with Pt nanoparticles produced hypergolically in a one-step reaction. The one-step hypergolic reaction to produce PtC catalysts is accomplished by mixing the metal precursor with sucrose (which serves as the carbon precursor) and adding sodium hydride as the igniting agent and reducing agent. The electrochemical performance of this material was also evaluated and benchmarked against the state-of-the-art commercial PtC. Interestingly, the hypergolically in situ-decorated carbon outperforms the analogous commercial PtC system.

2. EXPERIMENTAL SECTION

2.1. Materials. Platinum(IV) chloride, gold(III) chloride, silver nitrate, and sodium hydride were all purchased from Sigma-Aldrich. Sucrose (99%) was obtained from Alfa Aesar. Deionized water (18.2 MΩ cm at 25 °C) was produced by a Barnstead Pacific TII system and was used throughout the experiments. 40% platinum on Vulcan XC72 (carbon) was purchased from Fuel Cell Store. All chemicals were used as received without further purification.

2.2. Synthesis of Noble Metal Nanoparticles via Hypergolic Reactions. Safety note. All hypergolic reactions were carried out with small amounts of reagents by taking proper precautions and carrying out the reaction inside a fume hood with a ceramic tile bench.

All noble metal nanoparticles were synthesized in a similar manner using the corresponding metal salt precursor. For instance, for the Pt

https://doi.org/10.1021/acs.chemmater.4c02091
Chem. Mater. XXXX, XXX, XXX−XXX

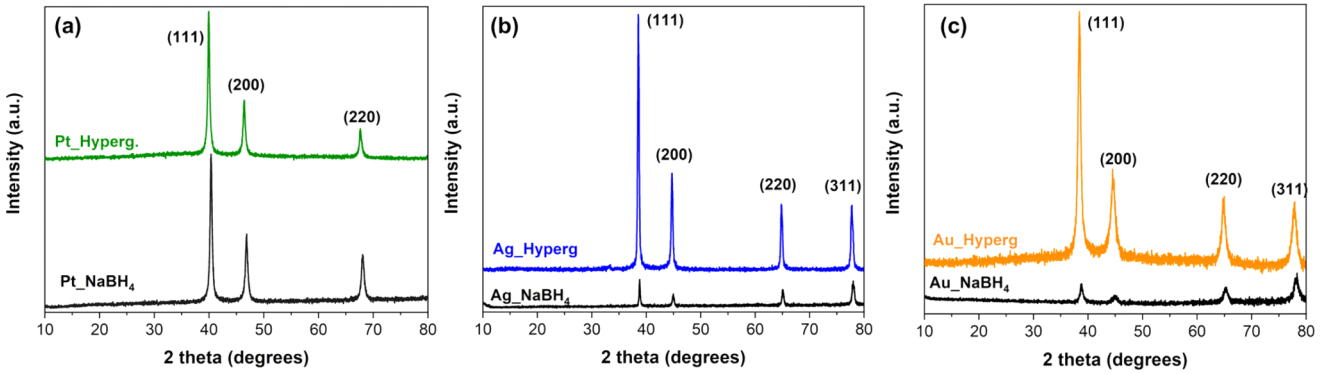

Figure 1. XRD patterns for the hypergolically and conventionally synthesized nanoparticles: (a) Pt, (b) Ag, and (c) Au.

nanoparticles, 0.5 g of platinum(IV) chloride was placed inside a glass test tube, followed by the addition of 1.5 mL of deionized water. A total of 0.5 g of solid sodium hydride NaH was added slowly in very small increments. After ignition, the product was recovered, washed with DI water and acetone, and dried.

2.3. Synthesis of AuPt Alloy via Hypergolic Reactions. 0.25 g portion of platinum(IV) chloride and 0.25 g of gold(III) chloride were placed inside a glass test tube and dissolved in 1.5 mL of deionized water. A total of 0.5 g of solid sodium hydride NaH was added slowly by using very small increments. After the ignition, the product was recovered, washed with DI water and acetone, and dried.

2.4. Synthesis of Noble Metal Nanoparticles with $NaBH_4$. 1.5 mmol of the corresponding metal salt precursor was added to 20 mL of deionized water followed by the addition of 20 mmol of solid $NaBH_4$. The solution was stirred for 1 h under ambient conditions. The final product was recovered, washed with DI water and acetone, and dried.

2.5. In Situ Decoration of a Carbon Substrate with Pt Nanoparticles. The one-step decoration involved dissolving in a glass test tube 2 g of sucrose in 2.2 mL of deionized water, followed by the addition of 0.25 g of platinum(IV) chloride. Sodium hydride was slowly added for ignition. After the reaction, the product was recovered, washed several times with DI water and acetone, and dried. The specific amounts used lead to a sample (referred to as PtC2) containing ~40% by weight of Pt on C.

Two more samples were prepared similarly. For the first, referred to as PtC1, 0.5 g of platinum(IV) chloride was used, while for the second, PtC3, 0.11 g of platinum(IV) chloride was used, leading to samples with ~70 and 30% by weight of Pt on C, respectively.

2.6. Characterization Techniques. XRD patterns were obtained with a D8 Advance diffractometer (Bruker AXS GmbH) using Cu Kα radiation (λ = 1.54 Å). Powder samples were deposited on background-free Si wafers and scanned over a 10−80° 2θ range in steps of 0.02° (2θ) and at a rate of 0.2 s per step. For easy comparisons, all XRD patterns were collected using equal amounts of sample. XPS spectra were measured by using a Thermo Scientific Nexsa G2 Spectrometer with an operating pressure of ca. 1×10^{-9} Torr. Monochromatic Al Kα X-rays (1486.6 eV) with photoelectrons were collected from a 200 μm diameter analysis spot at a 90° emission angle and a source-to-analyzer angle of 54.7°. A hemispherical analyzer determined the electron kinetic energy using a pass energy of 200 eV for wide/survey scans and 50 eV for high resolution scans. A flood gun was used for charge neutralization of nonconductive samples. The surface morphology along with chemical composition analysis was investigated by scanning electron microscopy (SEM) and energy dispersive X-ray spectroscopy (EDS) using a Zeiss Gemini 500 Scanning Electron Microscope. TEM images were collected using FEI Tecani 12 BioTwin TEM by preparing 1% w/v suspensions of the materials and drop-casting it into carbon-coated copper grids.

2.7. Electrochemical Measurements. The electrodes used for electrochemical measurements were made as follows. 6.0 mg of the particular electrocatalyst was mixed with 30 μL of a 2 wt % QAPPT solution in IPA and sonicated for approximately 30 min to form a homogeneous ink. 20 μL of the resulting ink was deposited onto a glassy carbon (GC) electrode (diameter = 5.0 mm, Pine Instrument) as the working electrode (WE) followed by thermal evaporation of the solvent under an infrared lamp. The catalyst loading was 0.2 mg cm^{-2}. An Ag/AgCl in saturated KCl solution, with a salt bridge separated from the WE, served as the reference electrode (RE) and a large-area graphite rod was used as the counter electrode (CE). The potential difference between Ag/AgCl in saturated KCl and the RHE in 0.1 M KOH was calculated from the Nernst equation. Electrochemical measurements were performed with a rotating disk electrode (RDE, Pine Instrument) in an oxygen-saturated 0.1 M KOH solution at room temperature, 1600 rpm, and a scan rate of 5 mV s^{-1}. ECSA was determined from hydrogen adsorption. A blank cyclic voltammogram (CV) in an Ar-saturated electrolyte from 0.08 to 1.12 V vs RHE at 5 mV s^{-1} was used. The activity of the Pt/HPC toward the oxygen reduction reaction (ORR) was measured in an O_2-saturated electrolyte in the same potential window at 5 mV/s and 1600 rpm. ECSA was calculated from the integration of the negative going potential scan from 0.5 to 0.075 V vs RHE, which corresponds to the charge of hydrogen adsorption, $Q_{H\text{-adsorption}}$, in eq1,

$$\mathrm{ECSA_{Pt}}\ (\mathrm{m^2\ g_{Pt}^{-1}}) = \left[\frac{Q_{H-\mathrm{adsorption}}(C)}{210\ \mu\mathrm{C\ cm_{Pt}^{-2}}\ L_{\mathrm{Pt}}(\mathrm{mg_{Pt}})}\right] \times 10^5 \quad (1)$$

where L_{Pt} is the loading of Pt on the GC electrode and 210 μC cm_{Pt}^{-2} is the charge of hydrogen adsorption on polycrystalline Pt.

An accelerated durability test (ADT) was conducted for 10 000 cycles between 0.6 and 1.1 V vs RHE with a scan rate of 500 mV s^{-1}. After 5000 cycles, the ORR was measured at 20 mV s^{-1} before another 5000 cycles of ADT were performed and the ORR activity was measured again.

3. RESULTS AND DISCUSSION

First, the phase purity and crystal structure of all nanoparticles were investigated by X-ray diffraction (XRD). Figure 1 shows the XRD patterns in the 10°−80° 2θ region for all nanoparticles synthesized hypergolically. For comparison, the corresponding XRD patterns of the nanoparticles synthesized conventionally using $NaBH_4$ in solution are also included. As shown in Figure 1, all nanoparticles synthesized hypergolically display intense and well-defined peaks. For the Pt nanoparticles, the diffraction peaks at 2θ = 39.9, 46.4, and 67.6° correspond to the (111), (200), and (220) reflections, respectively, consistent with the face-centered cubic (fcc) structure of crystalline platinum. The Ag nanoparticles show four prominent XRD diffraction peaks at 2θ = 38.5, 44.7, 64.8, and 77.7°, which can be assigned to (111), (200), (220), and (311), respectively, also consistent with a face-centered cubic crystal structure.[37] Similarly, in the case of Au, the four well-defined peaks present corresponding to the (111), (200),

https://doi.org/10.1021/acs.chemmater.4c02091
Chem. Mater. XXXX, XXX, XXX−XXX

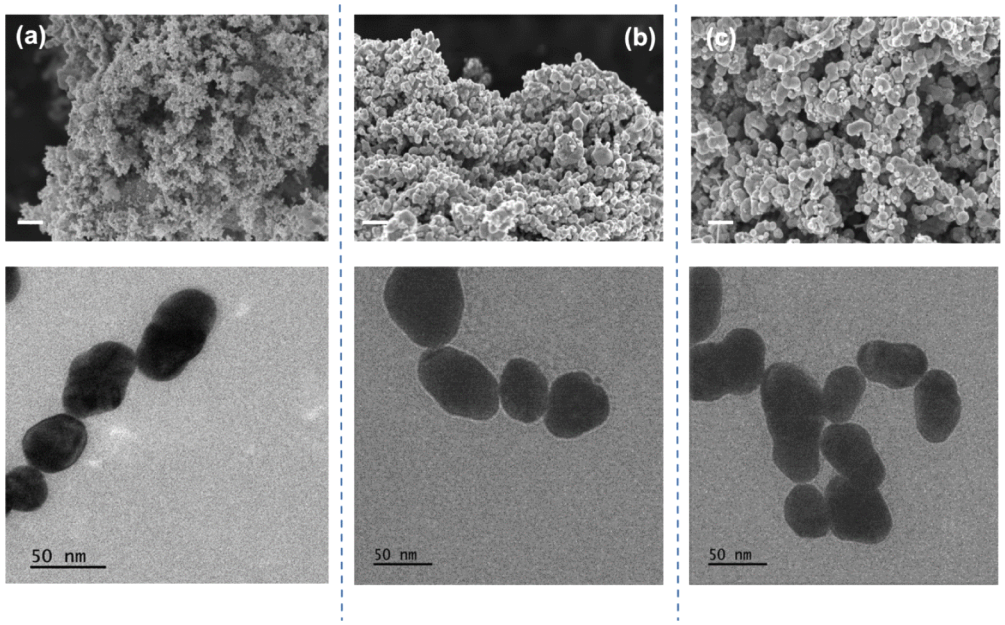

Figure 2. SEM and TEM images of (a) Pt, (b) Ag, and (c) Au NPs synthesized hypergolically. The scale bar in SEM images is 200 nm.

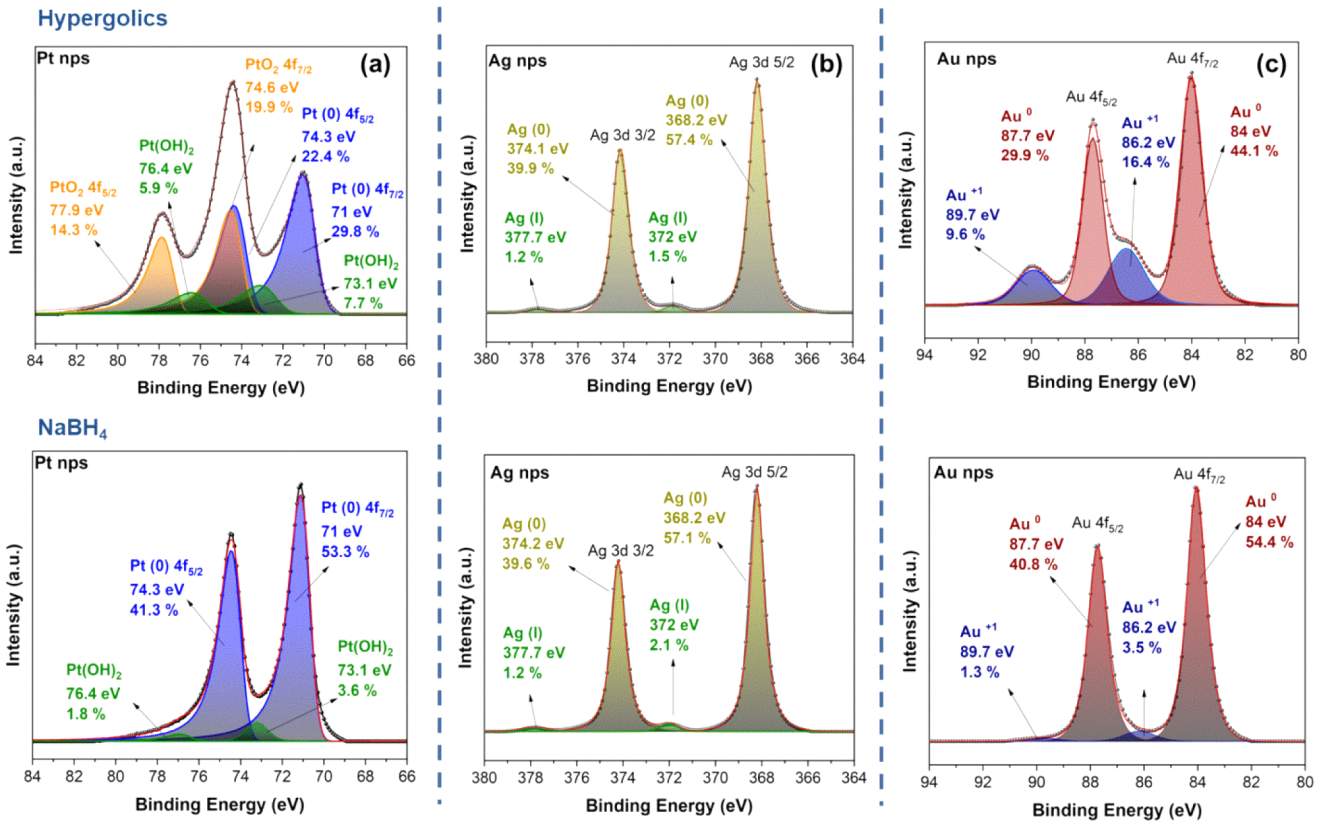

Figure 3. High-resolution XPS spectra of hypergolically (top) and conventionally (bottom) synthesized nanoparticles: (a) Pt 4f, (b) Ag 3d, and (c) Au 4f.

(220) and (311) reflections are consistent with a face-centered cubic lattice. Note that the conventionally synthesized nanoparticles display the same diffraction peaks, although their crystallinity is significantly reduced compared to that of the hypergolically derived particles.

Both TEM and SEM were further used to probe the morphology of the nanoparticles (Figure 2). The images reveal the presence of ellipsoidal nanoparticles, both individual and aggregated with relatively uniform sizes. In all cases, nanoparticles in the range of 30−50 nm were formed. In contrast, the conventionally synthesized nanoparticles using $NaBH_4$ display a more aggregated and wider size distribution especially in the case of Pt nanoparticles (Figure S1).

https://doi.org/10.1021/acs.chemmater.4c02091
Chem. Mater. XXXX, XXX, XXX−XXX

XPS was used to gain further insight into the chemical nature of all samples (Figure 3). For the hypergolically derived Pt nanoparticles, three different Pt species were detected (i.e., Pt(0), PtO_2, and $Pt(OH)_2$, corresponding to concentrations of 52.2, 34.2, and 13.6%, respectively) (Figure 3a). The oxidized Pt in the form of PtO_2 and $Pt(OH)_2$ is probably due to the fast reaction and quenching associated with the hypergolic reaction.[38,39] The conventionally synthesized nanoparticles, on the other hand, show mostly Pt metal and a smaller amount of oxidized Pt species present (<5.4%).[40] The high resolution spectrum of Ag 3d (Figure 3b) for the hypergolically derived and the conventionally synthesized nanoparticles shows metallic Ag as the dominant component (>96.5%) accompanied by a minor contribution of Ag(I) for both systems (Figure 3b). The high-resolution spectrum of the Au 4f core level (Figure 3c) shows two pairs of peaks due to Au $4f_{7/2}$ and Au $4f_{5/2}$ spin−orbit coupling. The first is related to elemental gold (Au^0), while the other is due to the stable gold oxide of Au^+.[41] From the spectra, we estimate the composition to be 74% for Au^0 and 26% for Au^{1+} for the hypergolically synthesized sample, while for the conventionally synthesized sample, the corresponding percentages are 95.2% and 4.8%, respectively.[41] While thermodynamics (redox potentials) suggest that gold and platinum should be reduced more readily than silver, the kinetics of oxidation and surface passivation differ. Silver oxides, once formed, can be reduced more quickly back to silver, while gold and platinum oxides might be more kinetically stable under the same reaction conditions. In addition, unlike gold and platinum nanoparticles, silver nanoparticles often form a stable passivation layer that prevents further oxidation. We note that the presence of additional oxidation states on the samples synthesized hypergolically might be an advantage and can be beneficial toward the electrochemical performance.[42]

Motivated by the unique conditions provided by the hypergolic reactions (localized heating, very fast reaction rates, and quenching), we explored the synthesis of nanoparticle alloys with the expectation that they might differ chemically or structurally from those produced conventionally under equilibrium conditions. Specifically, a AuPt alloy was prepared hypergolically using a mixture of the corresponding metal chloride salts (more details are provided in the experimental section). For comparison, we attempted to synthesize a similar alloy conventionally using a solution of $NaBH_4$, but instead of an alloy, a physical mixture of the two nanoparticles was produced. In contrast to the conventional reaction, the hypergolic reaction does lead to an alloy, as confirmed by the XRD pattern shown in Figure 4. For easy reference, the patterns of single Au and Pt were also included. The patterns are consistent with a face-centered cubic phase with the (111) and (200) diffraction peaks of the alloy falling between those for the individual Au and Pt nanoparticles. The *d*-spacing of the AuPt alloy (0.232 nm) is between that of Au (0.235 nm) and Pt (0.224 nm). We note that the diffraction peaks are broader and highly asymmetric. One can discern a main, relatively narrow peak superimposed on a broader background suggesting that, in addition to the main cubic phase, other phases with different chemical compositions yet being similar structurally are present due the fast quench of the reaction. These phases are assigned to alloys with an enriched platinum composition. As Au has a larger lattice constant than Pt, the latter metal can be subjected to tensile strain while Au would be under compression resulting in lattice distortion.[43]

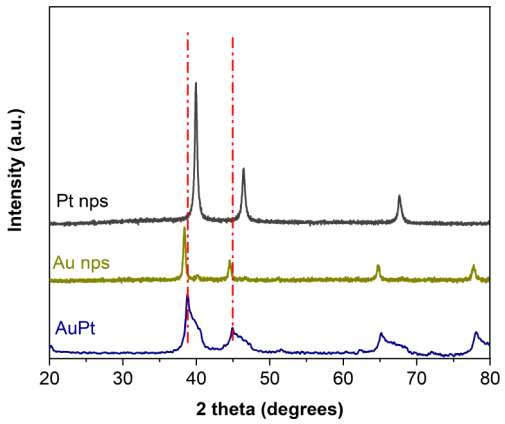

Figure 4. XRD patterns of the hypergolically synthesized 50:50 AuPt alloy. For comparison, the XRD patterns for Au and Pt nanoparticles are included.

Our results differ from previous reports of AuPt alloys prepared conventionally.[44] For instance, He et al. synthesized a series of AuPt alloys from similar precursors in aqueous solution using ascorbic acid as the reducing agent.[44] The XRD patterns for different compositions are characteristic of single phases, with the *d*-spacing varying linearly with the composition of the alloy. However, in their case, there seems to be one phase present for every composition rather than a series observed for our system.

Inspired by these observations, we set out to synthesize electrocatalysts in a one-step process, where both the carbon support and the nanoparticles are synthesized simultaneously rather than sequentially. The advantage of such samples is that they can lead to increased mass transfer and electrical conductivity of the catalytic layer and contribute to the stabilization of the metal nanoparticles.[45] Different ratios were explored to prepare a series of samples with varying amounts of Pt nanoparticles, as described in the experimental section. Of the different samples, we chose to characterize PtC2 in more detail because it closely corresponds to the state-of-the-art, commercially available electrocatalysts (40% platinum on Vulcan XC72), which is widely used in fuel cell systems.

The XRD pattern of PtC2 is shown in Figure S2a. Three intense peaks due to Pt nanoparticles and corresponding to the (111), (200), and (220) reflections are present, while a shoulder at 23° is attributed to disordered carbon[46] formed in situ from the sucrose. EDS spectra (Figure 5) show that the Pt loading in PtC2 is comparable to that of the commercially available electrocatalyst. Chemical mapping shows a uniform distribution of Pt nanoparticles (40 ± 3 wt %). The amount of oxygen in all cases is in the range of 10 wt %. Additional SEM images of PtC2 are shown in Figure S2b. We note that the platinum loading of the commercially available PtC electrocatalyst as determined by SEM-EDS is ~42 ± 2.5 wt % (Figure S3). The Pt loading on PtC1 and PtC3 were ~70 and 30% wt % (Figures S4 and S5), respectively. We finally note that the one-step synthesis leads to a similar uniform distribution of particles compared to the commercially available PtC electrocatalyst, as evidenced by the SEM-EDS (Figure 5).

Owing to our interest in developing alternative systems for electrocatalysis, we have evaluated the hypergollically synthesized nanoparticles and especially the in situ-decorated PtCs as electrocatalysts for ORR. AEMFCs have recently gained considerable interest due to their advantages over the currently

https://doi.org/10.1021/acs.chemmater.4c02091
Chem. Mater. XXXX, XXX, XXX−XXX

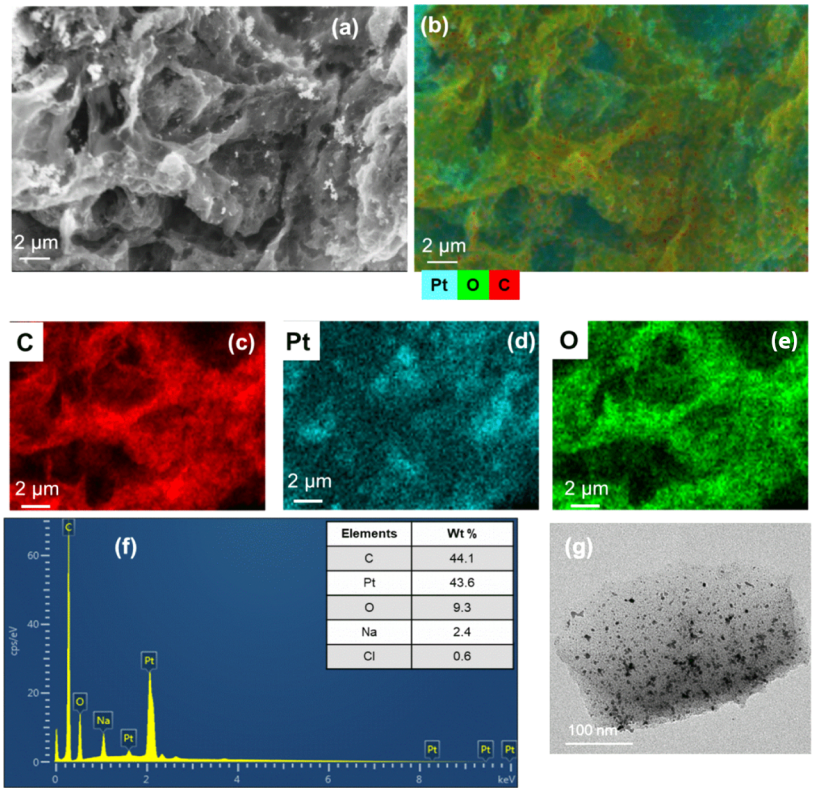

Figure 5. (a) SEM-EDS elemental map analysis: (a) electron image, (b) EDS-layered image, (c) C Kα, (d) Pt Kα, and (e) O Kα. Red is C, blue is Pt, and green is O. (f) Spectrum with corresponding weight composition and (g) TEM image of PtC2.

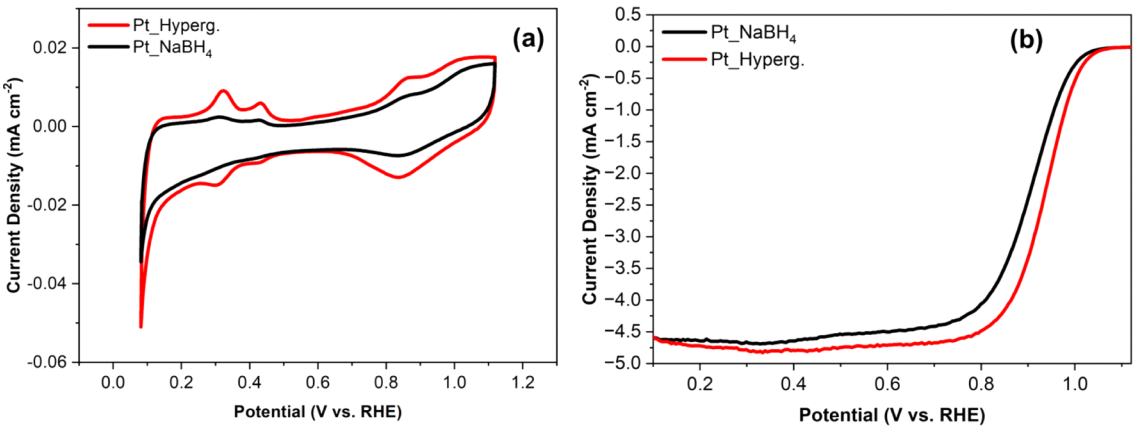

Figure 6. Electrochemical characterization of unsupported Pt NPs using RDE in 0.1 M KOH. (a) Cyclic voltammograms in Ar-saturated electrolyte and (b) polarization curves in an O_2-saturated electrolyte.

used PEMFCs.[47] While the two technologies share some common features, AEMFCs operate in an alkaline environments while PEMFCs operate in an acidic environment. AEMFCs offer several advantages, such as the use of a wider choice of fuels in addition to pure hydrogen and better oxygen reduction catalysis.[48] Moreover, in AEMFCs, the use of fluorinated compounds is not required, which are expensive and toxic.[49] ORR is faster in alkaline media as opposed to acidic conditions, allowing the use of electrodes with lower amounts of catalyst, which is of critical importance especially in noble metal-based catalyst systems.[50,51]

Despite efforts to find alternatives, Pt-based catalysts continue to be the systems of choice and are the benchmarks for the ORR for both AEMFCs and PEMFCs. To that end, we first present the results of the hypergolically prepared Pt nanoparticles. To measure the ESCA and the ORR activity, the unsupported Pt nanoparticles were tested in 0.1 M KOH in Ar- or O_2-saturated media, respectively. Quaternary ammonium poly(methylpiperidine-*co*-*p*-terphenyl), QAPPT, was used as a polymeric additive, since it possesses high OH^- conductivity (137 mS cm^{-1} at 80 °C) and is fairly stable in 1 M NaOH for more than 200 days.[52,53] The ECSA was determined by the hydrogen adsorption method by integrating the collected charges in the H adsorption region assuming 210 μC cm^{-2} for H monolayer adsorption (Figure 6a).[54]

The hypergolically derived unsupported nanoparticles show a more than double ECSA compared with the conventionally prepared Pt nanoparticles (13 versus 6 m^2 g_{Pt}^{-1}). We attribute

https://doi.org/10.1021/acs.chemmater.4c02091
Chem. Mater. XXXX, XXX, XXX−XXX

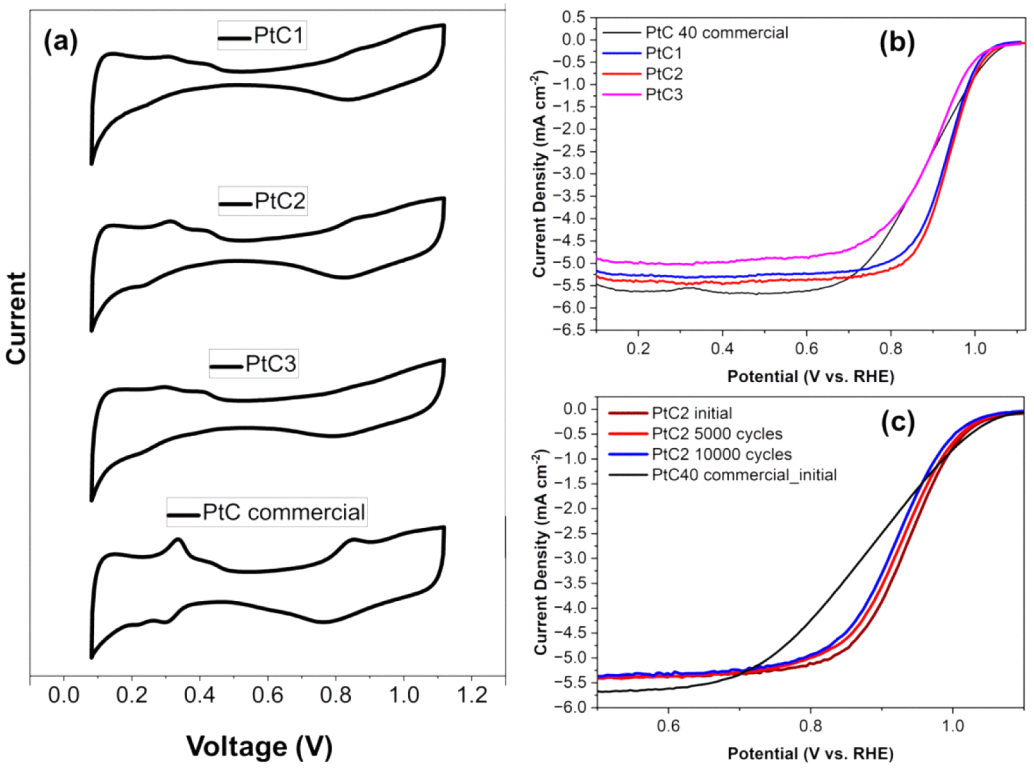

Figure 7. Electrochemical characterization of the in situ-decorated Pt NPs using RDE in 0.1 M KOH. (a) Cyclic voltammograms in Ar-saturated electrolyte, (b) polarization curves in the O_2-saturated electrolyte, and (c) ADT for PtC2.

the results to the smaller size of the hypergolically synthesized NPs resulting in higher electrochemically active area.[55] As expected, both samples (hypergolically and conventionally synthesized) show low ECSA values and limiting current compared to the state-of-the-art platinum-based catalysts because both were tested neat (i.e., not deposited on a support).[56] In the absence of support, the nanoparticles tend to agglomerate, limiting both the active sites and the charge transfer. The ORR activity of the hypergolically derived nanoparticles was ∼30 mV higher compared to the conventionally synthesized sample using $NaBH_4$, displaying an extremely high half-wave potential ($E_{1/2}$) of 0.94 V vs RHE (Figure 6b). $E_{1/2}$ constitutes one of the most critical parameters and is a widely used metric for evaluating ORR performance. It can be described as the required potential to reach half of the limiting current density obtained from the polarization curve. The higher the $E_{1/2}$ is, the lower overpotential to reach the specific current density, which corresponds to higher ORR performance.[57] Recall that $E_{1/2}$ is characteristic of the electroactive species present and it can be influenced by the oxidation states of the catalyst.[58]

Motivated by the significantly higher $E_{1/2}$ of the bare Pt nanoparticles, we moved to evaluate the ORR performance of the hypergolically, one-step-derived PtC catalysts. The generally accepted high-performance catalysts of carbon-supported Pt is attributed to the presence of electron vacancies by emptying the almost fully filled Pt 5d orbitals, when the platinum is dispersed. This feature is of critical importance to the high-performance of PtC electrocatalysts.[59] Electrocatalytic performance of the PtC catalysts was tested in 0.1 M KOH solution using the commercial 40 wt % PtC catalyst as baseline. ECSA is calculated by integrating the charges collected in the H adsorption region with the assumption of a H monolayer adsorption value of 210 μC cm^{-2} as stated previously. The ECSA is 40, 60, and 45 m^2 g_{Pt}^{-1} for PtC1, PtC2, and PtC3, respectively. The PtC2 sample with 60 m^2 g_{Pt}^{-1} shows the highest ECSA among the three samples and outperforms the commercial PtC catalyst (55 m^2 g_{Pt}^{-1}) with comparable Pt loading. We attribute the higher ECSA to the smaller size and the homogeneous distribution of Pt NPs in PtC2 (Figure 5g). PtC1 and PtC2 maintained a very high $E_{1/2}$ (0.94 V), while the PtC3 showed a comparable $E_{1/2}$ to the commercial electrocatalyst, PtC (0.9 V). However, PtC3 showed lower ECSA and limiting current probably due to the highly oxidized carbon as demonstrated by the C 1s spectrum (Figure S6). On the other hand, the limiting current of PtC1 and PtC2 is almost identical to the commercial PtC electrocatalyst. PtC1 and PtC2 showed almost identical C 1s spectra containing ∼25% C−O and C=O species (Figure S6). The corresponding level for PtC3 is 38%.

The higher $E_{1/2}$ of the hypergolically derived PtC1 and PtC2 samples compared to the commercial PtC, in addition to the smaller size of the nanoparticles, can be also attributed to the presence of different Pt oxidation states as shown in the deconvoluted high resolution Pt 4f spectrum (Figure 3). As stated previously, the presence of other oxidation states leads to better electrochemical performance.[42]

In order to evaluate the stability of the best performing sample (PtC2) toward ORR, an ADT was performed (Figure 7), which accelerates degradation to simulate conditions under long-term operation.[60] Although ADTs should be performed in a single fuel cell test station to effectively assess the performance degradation of the catalyst, half-cell tests through RDE are widely used to evaluate catalyst durability.[61,62] The $E_{1/2}$ reduction of the PtC2 catalyst is only ∼10 mV after 10 000 cycles. The corresponding value for the commercial PtC catalysts reported previously is ∼28 mV, making our catalysts

https://doi.org/10.1021/acs.chemmater.4c02091
Chem. Mater. XXXX, XXX, XXX−XXX

very attractive in terms of its stability and durability in alkaline environment.[63]

4. CONCLUSIONS

In summary, we demonstrate the first synthesis of noble metal nanoparticles using a hypergolic reactions. The approach involves reacting hypergolically the corresponding metal salt with sodium hydride acting as an exothermic ignition trigger as well as a reducing agent. In addition, we demonstrate that alloys can be formed when a mixture of metal salts is used. Finally, when sucrose is present along with the metal precursors, the reaction leads to carbon-supported nanoparticles in a one-step synthesis. The hypergolically derived nanoparticles display different oxidation states compared with the nanoparticles synthesized conventionally in solution and using $NaBH_4$ as the reducing agent. The presence of these oxidation states for the hypergolically synthesized systems leads to a better electrochemical performance. The in situ-synthesized carbon-supported Pt outperforms in terms of $E_{1/2}$ and durability of the state-of-the-art, commercial catalysts with a similar Pt loading. The reported approach leverages the unique experimental conditions of hypergolic reactions and provides an alternative strategy to design and synthesize new electrocatalysts with improved properties.

■ ASSOCIATED CONTENT

Supporting Information

The Supporting Information is available free of charge at https://pubs.acs.org/doi/10.1021/acs.chemmater.4c02091.

Representative SEM images of the conventionally synthesized nanoparticles (Figure S1); XRD pattern and additional SEM images of PtC2 (Figure S2); EDS chemical mapping of commercial carbon-supported platinum (40% platinum on Vulcan XC72) (Figure S3); EDS chemical mapping of PtC1 (Figure S4); EDS chemical mapping of PtC3 (Figure S5); high resolution C 1s spectra of (a) PtC1, (b) PtC2, and (c) PtC3 (Figure S6) (PDF)

■ AUTHOR INFORMATION

Corresponding Author

Emmanuel P. Giannelis − *Department of Materials Science and Engineering, Cornell University, Ithaca, New York 14850, United States*; Email: epg2@cornell.edu

Authors

Nikolaos Chalmpes − *Department of Materials Science and Engineering, Cornell University, Ithaca, New York 14850, United States*; orcid.org/0000-0003-2744-5934

Iosif Tantis − *Department of Materials Science and Engineering, Cornell University, Ithaca, New York 14850, United States*

Ahmed Wasel Alsmaeil − *Robert Frederick Smith School of Chemical and Biomolecular Engineering, Cornell University, Ithaca, New York 14850, United States*

Athanasios B. Bourlinos − *Physics Department, University of Ioannina, Ioannina 45110, Greece*

Complete contact information is available at: https://pubs.acs.org/10.1021/acs.chemmater.4c02091

Author Contributions

N.C. and E.P.G. conceived the project. N.C. synthesized, characterized, and analyzed all the samples. I.T. conducted the electrochemical characterizations. A.W.A. performed the TEM measurements. A.B.B. contributed to the mechanistic understanding of the study. N.C. wrote the manuscript. E.P.G. revised the manuscript.

Notes

The authors declare no competing financial interest.

■ ACKNOWLEDGMENTS

The authors acknowledge the support by the Center for Alkaline-based Energy Solutions (CABES), part of the Energy Frontier Research Center (EFRC) program supported by the U.S. Department of Energy, under grant DE-SC-0019445. The authors also acknowledge the use of facilities and instrumentation supported by NSF through the Cornell University Materials Research Science and Engineering Center DMR-1719875. The authors gratefully acknowledge Hector Abruña's group and especially Mihail Krumov from the Department of Chemistry and Chemical Biology for their help with the electrochemical characterization.

■ REFERENCES

(1) Sharma, J. N.; Pattadar, D. K.; Mainali, B. P.; Zamborini, F. P. Size determination of metal nanoparticles based on electrochemically measured surface-area-to-volume ratios. *Anal. Chem.* **2018**, *90*, 9308−9314.

(2) Kim, H.; Yoo, T. Y.; Bootharaju, M. S.; Kim, J. H.; Chung, D. Y.; Hyeon, T. Noble metal-based multimetallic nanoparticles for electrocatalytic applications. *Adv. Sci.* **2022**, *9* (1), 2104054.

(3) Gong, C.; Leite, M. S. Noble metal alloys for plasmonics. *ACS Photonics* **2016**, *3*, 507−513.

(4) Jain, P. K.; Huang, X.; El-Sayed, I. H.; El-Sayed, M. A. Noble metals on the nanoscale: optical and photothermal properties and some applications in imaging, sensing, biology, and medicine. *Acc. Chem. Res.* **2008**, *41*, 1578−1586.

(5) Theodosiou, M.; Chalmpes, N.; Gournis, D.; Sakellis, E.; Boukos, N.; Kostakis, M.; Thomaidis, N. S.; Efthimiadou, E. K. Amino acid driven synthesis of gold nanoparticles: A comparative study on their biocompatibility. *Mater. Chem. Phys.* **2024**, *319*, 129260.

(6) Stavropoulou, A. P.; Theodosiou, M.; Sakellis, E.; Boukos, N.; Papanastasiou, G.; Wang, C.; Tavares, A.; Corral, C. A.; Gournis, D.; Chalmpes, N.; Gobbo, O. L.; Efthimiadou, E. K. Bimetallic gold-platinum nanoparticles as a drug delivery system coated with a new drug to target glioblastoma. *Colloids Surf.* **2022**, *214*, 112463.

(7) Karageorgou, D.; Thomou, E.; Vourvou, N. T.; Lyra, K.-M.; Chalmpes, N.; Enotiadis, A.; Spyrou, K.; Katapodis, P.; Gournis, D.; Stamatis, H. Antibacterial and algicidal effects of porous carbon cuboid nanoparticles. *ACS Omega* **2019**, *4*, 4991−5001.

(8) Yahia-Ammar, A.; Sierra, D.; Mérola, F.; Hildebrandt, N.; Le Guével, X. Self-assembled gold nanoclusters for bright fluorescence imaging and enhanced drug delivery. *ACS Nano* **2016**, *10*, 2591−2599.

(9) Li, C.; Baek, J.-B. Recent advances in noble metal (Pt, Ru, and Ir)-based electrocatalysts for efficient hydrogen evolution reaction. *ACS Omega* **2020**, *5*, 31−40.

(10) Lv, Z.; He, S.; Wang, Y.; Zhu, X. Noble metal nanomaterials for NIR-triggered photothermal therapy in cancer. *Adv. Healthcare Mater.* **2021**, *10* (6), 2001806.

(11) Geng, H.; Vilms Pedersen, S.; Ma, Y.; Haghighi, T.; Dai, H.; Howes, P. D.; Stevens, M. M. Noble metal nanoparticle biosensors: from fundamental studies toward point-of-care diagnostics. *Acc. Chem. Res.* **2022**, *55*, 593−604.

(12) Jamkhande, P. G.; Ghule, N. W.; Bamer, A. H.; Kalaskar, M. G. Metal nanoparticles synthesis: an overview on methods of

preparation, advantages and disadvantages, and applications. *J. Drug Deliv. Sci. Technol.* **2019**, *53*, 101174.
(13) Habibullah, G.; Viktorova, J.; Ruml, T. Current strategies for noble metal nanoparticle synthesis. *Nanoscale Res. Lett.* **2021**, *16* (1), 47.
(14) Karageorgou, D.; Zygouri, P.; Tsakiridis, T.; Hammami, M. A.; Chalmpes, N.; Subrati, M.; Sainis, I.; Spyrou, K.; Katapodis, P.; Gournis, D.; Stamatis, H. Green synthesis and characterization of silver nanoparticles with high antibacterial activity using cell extracts of cyanobacterium pseudanabaena/limnothrix sp. *Nanomaterials* **2022**, *12*, 2296.
(15) de Oliveira, P. F. M.; Torresi, R. M.; Emmerling, F.; Camargo, P. H. C. Challenges and opportunities in the bottom-up mechanochemical synthesis of noble metal nanoparticles. *J. Mater. Chem. A* **2020**, *8*, 16114−16141.
(16) Wang, T.; Aguey-Zinsou, K.-F. Surfactant-free" sodium borohydride nanoparticles with enhanced hydrogen desorption properties. *ACS Appl. Energy Mater.* **2020**, *3*, 9940−9949.
(17) Iordache, M.; Oubraham, A.; Sorlei, I.-S.; Lungu, F. A.; Capris, C.; Popescu, T.; Marinoiu, A. Noble metals functionalized on graphene oxide obtained by different methods—new catalytic materials. *Nanomaterials* **2023**, *13*, 783.
(18) Chen, J. P.; Lim, L. L. Key factors in chemical reduction by hydrazine for recovery of precious metals. *Chemosphere* **2002**, *49*, 363−370.
(19) Ranoszek-Soliwoda, K.; Tomaszewska, E.; Socha, E.; Krzyczmonik, P.; Ignaczak, A.; Orlowski, P.; Krzyzowska, M.; Celichowski, G.; Grobelny, J. The role of tannic acid and sodium citrate in the synthesis of silver nanoparticles. *J. Nanopart. Res.* **2017**, *19* (8), 273.
(20) Zhao, L.; Zhu, J.; Zheng, Y.; Xiao, M.; Gao, R.; Zhang, Z.; Wen, G.; Dou, H.; Deng, Y.-P.; Yu, A.; et al. Materials engineering toward durable electrocatalysts for proton exchange membrane fuel cells. *Adv. Energy Mater.* **2022**, *12* (2), 2102665.
(21) Tian, X. L.; Xu, Y. Y.; Zhang, W.; Wu, T.; Xia, B. Y.; Wang, X. Unsupported platinum-based electrocatalysts for oxygen reduction reaction. *ACS Energy Lett.* **2017**, *2*, 2035−2043.
(22) Kodama, K.; Nagai, T.; Kuwaki, A.; Jinnouchi, R.; Morimoto, Y. Challenges in applying highly active Pt-based nanostructured catalysts for oxygen reduction reactions to fuel cell vehicles. *Nat. Nanotechnol.* **2021**, *16*, 140−147.
(23) Tuaev, X.; Rudi, S.; Strasser, P. The impact of the morphology of the carbon support on the activity and stability of nanoparticle fuel cell catalysts. *Catal. Sci. Technol.* **2016**, *6*, 8276−8288.
(24) Ott, S.; Orfanidi, A.; Schmies, H.; Anke, B.; Nong, H. N.; Hübner, J.; Gernert, U.; Gliech, M.; Lerch, M.; Strasser, P. Ionomer distribution control in porous carbon-supported catalyst layers for high-power and low Pt-loaded proton exchange membrane fuel cells. *Nat. Mater.* **2020**, *19*, 77−85.
(25) Bayan, Y.; Paperzh, K.; Pankov, I.; Alekseenko, A. Influence of a carbon support on the catalytic activity and durability of the Pt-based electrocatalysts. *Mater. Lett.* **2024**, *368*, 136670.
(26) Tian, X. L.; Wang, L.; Deng, P.; Chen, Y.; Xia, B. Y. Research advances in unsupported Pt-based catalysts for electrochemical methanol oxidation. *J. Energy Chem.* **2017**, *26*, 1067−1076.
(27) Li, Y.; Guo, S. Noble metal-based 1D and 2D electrocatalytic nanomaterials: recent progress, challenges and perspectives. *Nano Today* **2019**, *28*, 100774.
(28) Chalmpes, N.; Bourlinos, A. B.; Alsmaeil, A. W.; Aljarrah, A. S.; Salmas, C. E.; Karakassides, M. A.; Giannelis, E. P. First synthesis of 2D materials by hypergolic reactions and evaluation of their dispersions for ink formulation: hexagonal boron nitride and fluorinated carbon nanosheets. *Mater. Res. Express* **2024**, *11*, 035002.
(29) Chalmpes, N.; Spyrou, K.; Vasilopoulos, K. C.; Bourlinos, A. B.; Moschovas, D.; Avgeropoulos, A.; Gioti, C.; Karakassides, M. A.; Gournis, D. Hypergolics in carbon nanomaterials synthesis: new paradigms and perspectives. *Molecules* **2020**, *25*, 2207.
(30) Baikousi, M.; Chalmpes, N.; Spyrou, K.; Bourlinos, A. B.; Avgeropoulos, A.; Gournis, D.; Karakassides, M. A. Direct production of carbon nanosheets by self-ignition of pyrophoric lithium dialkylamides in air. *Mater. Lett.* **2019**, *254*, 58−61.
(31) Chalmpes, N.; Asimakopoulos, G.; Spyrou, K.; Vasilopoulos, K. C.; Bourlinos, A. B.; Moschovas, D.; Avgeropoulos, A.; Karakassides, M. A.; Gournis, D. Functional carbon materials derived through hypergolic reactions at ambient conditions. *Nanomaterials* **2020**, *10*, 566.
(32) Bourlinos, A. B.; Chalmpes, N.; Gournis, D.; Karakassides, M. A. Hypergolic materials synthesis: a review. *J. Nanotechnol. Res.* **2022**, *04* (02), 59−96.
(33) Chalmpes, N.; Bourlinos, A. B.; Šedajová, V.; Kupka, V.; Moschovas, D.; Avgeropoulos, A.; Karakassides, M. A.; Gournis, D. Hypergolic materials synthesis through reaction of fuming nitric acid with certain cyclopentadienyl compounds. *C* **2020**, *6*, 61.
(34) Chalmpes, N.; Moschovas, D.; Tantis, I.; Bourlinos, A. B.; Bakandritsos, A.; Fotiadou, R.; Patila, M.; Stamatis, H.; Avgeropoulos, A.; Karakassides, M. A.; Gournis, D. Carbon nanostructures derived through hypergolic reaction of conductive polymers with fuming nitric acid at ambient conditions. *Molecules* **2021**, *26*, 1595.
(35) Mädler, L.; Kammler, H. K.; Mueller, R.; Pratsinis, S. E. Controlled synthesis of nanostructured particles by flame spray pyrolysis. *J. Aerosol Sci.* **2002**, *33*, 369−389.
(36) Pratsinis, S. E. Simultaneous nucleation, condensation, and coagulation in aerosol reactors. *J. Colloid Interface Sci.* **1988**, *124*, 416−427.
(37) Jyoti, K.; Baunthiyal, M.; Singh, A. Characterization of silver nanoparticles synthesized using Urtica dioica Linn. leaves and their synergistic effects with antibiotics. *J. Radiat. Res. Appl. Sci.* **2016**, *9*, 217−227.
(38) Banerjee, R.; Chen, D. A.; Karakalos, S.; Piedboeuf, M.-L. C.; Job, N.; Regalbuto, J. R. Ambient oxidation of ultrasmall platinum nanoparticles on microporous carbon catalyst supports. *ACS Appl. Nano Mater.* **2018**, *1*, 5876−5884.
(39) Dong, C.; Lian, C.; Hu, S.; Deng, Z.; Gong, J.; Li, M.; Liu, H.; Xing, M.; Zhang, J. Size-dependent activity and selectivity of carbon dioxide photocatalytic reduction over platinum nanoparticles. *Nat. Commun.* **2018**, *9* (1), 1252.
(40) Şen, F.; Gökağaç, G. Different Sized Platinum Nanoparticles Supported on Carbon: An XPS study on these methanol oxidation Catalysts. *J. Phys. Chem. C* **2007**, *111*, 5715−5720.
(41) Maack, I.; Osmić, M.; Mohrhusen, L.; Buhani, P.; Al-Shamery, K. Fitting a qquare peg into a round hole: shape control in phase transfer of cubic gold nanoparticles. *ChemNanomat* **2021**, *7*, 658−671.
(42) Wang, C.; Jiu, H.; Song, W.; Shi, R.; Che, S.; Han, Y.; Guo, Z.; Li, H.; Ma, J.; Zhang, L. Bi nanoparticles with different oxidation states embedded in porous carbon nanosheets as high-performance anode for lithium-ion battery. *J. Alloys Compd.* **2023**, *960*, 170969.
(43) García-Negrete, C. A.; Knappett, B. R.; Schmidt, F. P.; Rojas, T. C.; Wheatley, A. E. H.; Hofer, F.; Fernández, A. Island-type growth of Au−Pt heterodimers: direct visualization of misfit dislocations and strain-relief mechanisms. *RSC Adv.* **2015**, *5*, 55262−55268.
(44) He, W.; Han, X.; Jia, H.; Cai, J.; Zhou, Y.; Zheng, Z. AuPt alloy nanostructures with tunable composition and enzyme-like activities for colorimetric detection of bisulfide. *Sci. Rep.* **2017**, *7* (1), 40103.
(45) Dong, Y.; Li, H.; Mei, X.; Han, C.; Gong, X.; Song, P.; Xu, W. Synergetic effect between platinum nanoparticles and single atoms revealed in the catalytic mechanism of traditional Pt/C for the oxygen reduction reaction. *ACS Appl. Energy Mater.* **2024**, *7*, 5352−5358.
(46) Chalmpes, N.; Tantis, I.; Bakandritsos, A.; Bourlinos, A. B.; Karakassides, M. A.; Gournis, D. Rapid carbon formation from spontaneous reaction of ferrocene and liquid bromine at ambient conditions. *Nanomaterials* **2020**, *10*, 1564.
(47) Jiao, K.; Xuan, J.; Du, Q.; Bao, Z.; Xie, B.; Wang, B.; Zhao, Y.; Fan, L.; Wang, H.; Hou, Z.; Huo, S.; Brandon, N. P.; Yin, Y.; Guiver, M. D. Designing the next generation of proton-exchange membrane fuel cells. *Nature* **2021**, *595*, 361−369.
(48) Ricciardi, B.; Mecheri, B.; da Silva Freitas, W.; Ficca, V. C. A.; Placidi, E.; Gatto, I.; Carbone, A.; Capasso, A.; D'Epifanio, A. Porous

https://doi.org/10.1021/acs.chemmater.4c02091
Chem. Mater. XXXX, XXX, XXX−XXX

iron-nitrogen-carbon electrocatalysts for anion exchange membrane fuel cells (AEMFC). *ChemElectrochem* **2023**, *10* (7), No. e202201115.
(49) Santori, P. G.; Mondal, A. N.; Dekel, D. R.; Jaouen, F. The critical importance of ionomers on the electrochemical activity of platinum and platinum-free catalysts for anion-exchange membrane fuel cells. *Sustain. Energy Fuels* **2020**, *4*, 3300−3307.
(50) Firouzjaie, H. A.; Mustain, W. E. Catalytic advantages, challenges, and priorities in alkaline membrane fuel cells. *ACS Catal.* **2020**, *10*, 225−234.
(51) Ramaswamy, N.; Mukerjee, S. Fundamental mechanistic understanding of electrocatalysis of oxygen reduction on Pt and non-Pt surfaces: acid versus alkaline media. *Adv. Phys. Chem.* **2012**, *2012*, 491604.
(52) Chen, N.; Lee, Y. M. Anion exchange polyelectrolytes for membranes and ionomers. *Prog. Polym. Sci.* **2021**, *113*, 101345.
(53) Zhou, Y.; Yu, H.; Xie, F.; Zhao, Y.; Sun, X.; Yao, D.; Jiang, G.; Geng, J.; Shao, Z. Improving cell performance for anion exchange membrane fuel cells with FeNC cathode by optimizing ionomer content. *Int. J. Hydrogen Energy* **2023**, *48*, 5266−5275.
(54) Garsany, Y.; Baturina, O. A.; Swider-Lyons, K. E.; Kocha, S. S. Experimental methods for quantifying the activity of platinum electrocatalysts for the oxygen reduction reaction. *Anal. Chem.* **2010**, *82*, 6321−6328.
(55) Men Truong, V.; Richard Tolchard, J.; Svendby, J.; Manikandan, M.; Miller, A. H.; Sunde, S.; Yang, H.; Dekel, R. D.; Oyarce Barnett, A. Platinum and platinum group metal-free catalysts for anion exchange membrane fuel cells. *Energies* **2020**, *13* (3), 582.
(56) Xu, Z.; Zhang, H.; Zhong, H.; Lu, Q.; Wang, Y.; Su, D. Effect of particle size on the activity and durability of the Pt/C electrocatalyst for proton exchange membrane fuel cells. *Appl. Catal., B* **2012**, *111*−*112*, 264−270.
(57) Wang, J.; Zhao, C.-X.; Liu, J.-N.; Ren, D.; Li, B.-Q.; Huang, J.-Q.; Zhang, Q. Quantitative kinetic analysis on oxygen reduction reaction: A perspective. *NMS* **2021**, *3*, 313−318.
(58) Pietrzyk, D. J.; Frank, C. W. Chapter Twenty-Nine - Polarography. In *Analytical Chemistry*; Pietrzyk, D. J.; Frank, C. W., Eds.; Academic Press, 1979; pp. 598613.
(59) Xiao, Y.-X.; Ying, J.; Chen, J.-B.; Dong, Y.; Yang, X.; Tian, G.; Wu, J.; Janiak, C.; Ozoemena, K. I.; Yang, X.-Y. Confined ultrafine Pt in porous carbon fibers and their N-enhanced heavy d-π effect. *Chem. Mater.* **2022**, *34*, 3705−3714.
(60) Messing, M.; Kjeang, E. Empirical modeling of cathode electrode durability in polymer electrolyte fuel cells. *J. Power Sources* **2020**, *451*, 227750.
(61) Riese, A.; Banham, D.; Ye, S.; Sun, X. Accelerated stress testing by rotating disk electrode for carbon corrosion in fuel cell catalyst supports. *J. Electrochem. Soc.* **2015**, *162*, F783.
(62) Nagai, T.; Jahn, C.; Jia, H. Improved Accelerated stress tests for ORR catalysts using a rotating disk electrode. *J. Electrochem. Soc.* **2019**, *166*, F3111.
(63) Cai, J.; Chen, J.; Chen, Y.; Zhang, J.; Zhang, S. Engineering carbon semi-tubes supported platinum catalyst for efficient oxygen reduction electrocatalysis. *iScience* **2023**, *26*, 106730.

https://doi.org/10.1021/acs.chemmater.4c02091
Chem. Mater. XXXX, XXX, XXX−XXX